Ephemeral antibubbles: Spatiotemporal evolution from direct numerical simulations

Nairita Pal,[1,*] Rashmi Ramadugu,[2,†] Prasad Perlekar,[2,‡] and Rahul Pandit[3,§]

[1]*Center for Oceans, Rivers, Atmosphere and Land Sciences, Indian Institute of Technology, Kharagpur, Kharagpur 721302, India*
[2]*TIFR Center for Interdisciplinary Sciences, Tata Institute of Fundamental Research, Gopanpally, Hyderabad 500046, India*
[3]*Centre for Condensed Matter Theory, Department of Physics, Indian Institute of Science, Bangalore 560012, India*

(Received 7 April 2021; accepted 6 October 2022; published 22 November 2022)

Antibubbles, which consist of a shell of a low-density fluid inside a high-density fluid, have several promising applications. We show, via extensive direct numerical simulations (DNSs), in both two and three dimensions, that the spatiotemporal evolution of antibubbles can be described naturally by the coupled Cahn-Hilliard-Navier-Stokes (CHNS) equations for a binary fluid. Our DNSs capture elegantly the gravity-induced thinning and breakup of an antibubble via the time evolution of the Cahn-Hilliard scalar-order-parameter field ϕ, which varies continuously across interfaces, so we do not have to enforce complicated boundary conditions at the moving antibubble interfaces. To ensure that our results are robust, we supplement our CHNS simulations with sharp-interface volume-of-fluid DNSs. We track the thickness of the antibubble and calculate the dependence of the lifetime of an antibubble on several parameters; we show that our DNS results agree with various experimental results; in particular, the velocity with which the arms of the antibubble retract after breakup scales as $\sigma^{1/2}$, where σ is the surface tension.

DOI: 10.1103/PhysRevResearch.4.043128

I. INTRODUCTION

Antibubbles, which comprise a shell of a low-density fluid inside a high-density fluid, have been known for close to 90 years, since the work of Hughes and Hughes [1]. In contrast to an ordinary bubble, an antibubble has two surfaces, which trap a certain volume of fluid between them. Therefore, the contact area of an antibubble is much larger than that of a bubble with the same fluid volume; this property can be exploited for a variety of chemical reactions. Furthermore, antibubbles are commonly used in clinical diagnostic imaging, sonoporation (see, e.g., Ref. [2]), as agents for ultrasound-guided drug delivery [3–5], and for active leakage detection [6]. Clearly, an antibubble is unstable in the presence of gravity, and, if the inner core of the antibubble is denser than the outer core, the antibubble rises under gravity; because of hydrostatic pressure in the outer core, the fluid rises from the bottom to the top, resulting in a thinning, and subsequent collapse, of the shell. Although there have been a number of experimental investigations of the spatiotemporal evolution of an antibubble [7–15] and drops [16–20] to name a few, over the past few decades, theoretical studies of antibubble evolution have been initiated only recently [15,21–25] and they have not attempted, hitherto, to address the spatiotemporal evolution of antibubbles in detail. The number of experimental studies of the complete spatiotemporal evolution of antibubbles is also limited, partly because great care has to be exercised to stabilize antibubbles; often, surfactant molecules have to be introduced into the high-density liquid phase for such stabilization.

We develop a *natural, multiphase* model for antibubbles and demonstrate how we can use direct numerical simulations (DNSs) to follow the spatiotemporal development of ephemeral, but beautiful, antibubbles. We show that the Cahn-Hilliard-Navier-Stokes (CHNS) equations, which have been used to study a variety of problems in binary-fluid flows [26–35], provide a *minimal theoretical framework* for studying the spatiotemporal evolution of antibubbles; in addition to a velocity field, the CHNS system employs a phase field ϕ that distinguishes between the two fluid phases. We use the CHNS equations [26,27,29–32] to study antibubbles in two dimensions (2D) and in three dimensions (3D) by using extensive DNSs. To complement our CHNS results, we also employ an alternative volume-of-fluid (VF) numerical scheme that is a sharp-interface method.

Our studies yield several interesting results that (a) provide explanations for many experimental observations and (b) suggest new experimental studies: Our results for the spatiotemporal evolution of antibubbles, in 2D and 3D, show clearly how antibubble breakup occurs either because of gravity-induced thinning or the puncturing of its bottom boundary; the collapsing antibubble then forms a rim that retracts with a velocity $v_{\rm rim}$. We uncover signatures of this collapse in Fourier-space spectra of (a) the Fourier transform $\hat{\phi}$ of the Cahn-Hilliard field, (b) the velocity, and (c) the

*nairitap2009@gmail.com
†rashmi.ramadugu@gmail.com
‡perlekar@tifrh.res.in
§rahul@iisc.ac.in; also at Jawaharlal Nehru Centre For Advanced Scientific Research, Jakkur, Bangalore, India.

vorticity. We show that $v_{\rm rim} \sim \sigma^{1/2}$, where σ is the surface tension, and this power-law exponent is independent of the kinematic viscosity ν of the background fluid. We investigate the dependence of the scaled antibubble lifetime τ_1/τ_g on σ, ν, and the scaled outer radius of the antibubble R_0/h_0, in 2D; here, $\tau_g \equiv \sqrt{R_0/Ag}$, with A the Atwood number and g the acceleration due to gravity, and h_0 is the initial thickness of the antibubble shell. We compare our results with experiments and earlier theoretical studies.

The remainder of this paper is organized as follows. In Sec. II we present the models and the numerical methods that we use. In Sec. III we present the results of our DNSs in the following subsections: subsection III A on the spatiotemporal evolution of antibubbles (2D DNSs); subsection III B on the temporal evolution of Fourier spectra of ϕ and the velocity and vorticity fields that are associated with antibubbles in our 2D DNSs; subsection III C on the velocity of the retracting rim of the ruptured antibubble in our 2D DNSs; subsection III D on the signatures of this rupture in the time dependence of the energy; subsection III E 1 on the dependence of the antibubble-rupture time on the size of the antibubble and the surface tension; subsection III E 2 on the dependence of the antibubble-rupture time on the kinematic viscosity; subsection III F on the spatiotemporal evolution of antibubbles in our 3D DNSs. We present conclusions and a discussion of our results in Sec. IV.

II. MODEL AND NUMERICAL METHODS

An antibubble consists of a shell of light fluid of density ρ_1 inside a background heavy fluid of density ρ_2; these fluids are immiscible and incompressible. The following CHNS equations provide a natural theoretical description for such a binary-fluid mixture [36–39]:

$$\rho(\phi)D_t\boldsymbol{u} = -\nabla p + \varsigma(\phi)\nabla^2\boldsymbol{u} + \mathbf{F}_\sigma + \left[\rho(\phi) - \frac{\rho_1+\rho_2}{2}\right]\boldsymbol{g} - \alpha\mathbf{u}, \tag{1}$$

$$D_t\phi = \gamma\nabla^2\mu, \quad \nabla\cdot\boldsymbol{u} = 0. \tag{2}$$

In Eqs. (1) and (2), $D_t \equiv (\partial_t + \boldsymbol{u}\cdot\nabla)$ is the convective derivative, $\boldsymbol{u} \equiv (u_x, u_y, u_z)$ is the fluid velocity, α is the coefficient of friction (we use this only in 2D; physically, it can be thought of as a contact friction coming from a surface or planar drag, e.g., wind drag on the plane), $\boldsymbol{g}$ is the constant acceleration due to gravity, which points downwards, $\rho(\phi) \equiv \rho_1(1+\phi)/2 + \rho_2(1-\phi)/2$ is the density, $\varsigma(\phi) \equiv \nu_1(1+\phi)/2 + \nu_2(1-\phi)/2$ is the dynamic viscosity, and $\phi(\boldsymbol{x}, t)$ is the order-parameter field at the point $\boldsymbol{x}$ and time t [with $\phi(\boldsymbol{x}, t) < 0$ in the background (majority) phase and $\phi(\boldsymbol{x}, t) > 0$ in the antibubble-shell (minority) phase]. Here, ν_1 is the viscosity of the minority or the antibubble phase ($\phi > 0$) and ν_2 is the viscosity of the majority or the background phase ($\phi < 0$). Thus the net viscosity $\varsigma(\phi)$ is positive.

When we study 2D flows, we use the following stream-function-vorticity formulation [26,40]:

$$(\partial_t + \boldsymbol{u}\cdot\nabla)\omega = \nu\nabla^2\omega - \alpha\omega - \nabla\times(\phi\nabla\mu) - A\nabla\phi\times\boldsymbol{g},$$
$$(\partial_t + \boldsymbol{u}\cdot\nabla)\phi = \gamma\nabla^2\mu, \quad \nabla\cdot\boldsymbol{u} = 0. \tag{3}$$

Here, $\boldsymbol{\omega} = (\nabla\times\boldsymbol{u})$ is the vorticity; in our 2D simulations, $\boldsymbol{u} = (u_x, u_y, 0)$, so $\boldsymbol{\omega} = \omega\hat{\boldsymbol{e}}_z$. We obtain $\omega(\boldsymbol{x}, t)$ and $\phi(\boldsymbol{x}, t)$ from our 2D DNS, and from these we calculate the total kinetic energy $E(t) = \langle|\boldsymbol{u}(\boldsymbol{x}, t)|^2\rangle_{\boldsymbol{x}}$ and the fluid-energy dissipation rate $\varepsilon(t) = \langle\nu|\omega(\boldsymbol{x}, t)|^2\rangle_{\boldsymbol{x}}$, where $\langle\rangle_{\boldsymbol{x}}$ denotes the average over space. We calculate the lifetime of an antibubble falling under gravity in two ways: (a) From the energy time series and (b) from the minimum thickness at the South pole of the antibubble.

At time $t = 0$ we begin with the order-parameter profile [36]

$$\phi(\boldsymbol{x}) = -\tanh\left[\frac{1}{\sqrt{2}\xi}(|\boldsymbol{x}-\boldsymbol{x}_c| - R_0)\right] + \tanh\left[\frac{1}{\sqrt{2}\xi}(|\boldsymbol{x}-\boldsymbol{x}_c| - R_1)\right] - 1.0, \tag{4}$$

where R_0 and R_1 are, respectively, the initial magnitudes of the outer and inner radii of the antibubble, whose center is initially at $\boldsymbol{x}_c$; the interface width ξ is measured by the dimensionless Cahn number $Ch = \xi/L$, where L $(= 2\pi)$ is the linear size of our simulation domain. In our study, the Cahn number is just a constant fixed at $t = 0$ and is not a dynamical quantity representing any physics of the system. We have used $L = 2\pi$ as the box size and the interface width is nondimensionalized with this constant value of 2π. Alternatively, we could have used some dynamical quantity (e.g., the integral length scale of the system) if we wished the Cahn number to reflect the dynamics of the system. But this is not our purpose here and is beyond the scope of the current work. The interface width ξ is the length over which ϕ changes from its value in the majority phase to that in the majority phase at $t = 0$. Of course, if ξ is large relative to R_0 and R_1, a ring shape will not be observed. In particular, for such a ring to appear, ξ must be smaller than the thickness h_0 of the antibubble, i.e., $h_0/\xi > 1$. To avoid numerical artifacts, we choose parameters such that $\xi \simeq 3dx$, where dx is the resolution of our spatial grid. We use the initial thickness of the antibubble shell $h_0 \equiv R_0 - R_1$ as a typical length scale.

In our CHNS studies we use the Boussinesq approximation, wherein $\rho(\phi)D_t\boldsymbol{u} \approx \frac{\rho_1+\rho_2}{2}D_t\boldsymbol{u}$ and $[\rho(\phi) - \frac{\rho_1+\rho_2}{2}]\boldsymbol{g} \approx -A(\frac{\rho_1+\rho_2}{2})\phi g$ in Eq. (1), where $A = (\rho_1 - \rho_2)/(\rho_2 + \rho_1)$ is the Atwood number; the surface-tension force $\mathbf{F}_\sigma \equiv -\phi\nabla\mu$ and the chemical potential $\mu(\boldsymbol{x}, t)$ follow from the Cahn-Hilliard free-energy functional $\mathcal{F}$:

$$\mathcal{F}[\phi] = \Lambda\int[(\phi^2-1)^2/(4\xi^2) + |\nabla\phi|^2/2]d\boldsymbol{x},$$
$$\mu = \delta\mathcal{F}[\phi]/\delta\phi(\boldsymbol{x}, t). \tag{5}$$

Here, Λ is the energy density with which the two phases mix in the interfacial regime [36], ξ sets the scale of the interface width, $\sigma = \frac{2\sqrt{2}\Lambda}{3\xi}$ is the surface tension, and γ is the mobility [38] of the binary-fluid mixture; the Schmidt number $Sc = \nu/D$. We assume that γ and ρ are independent of ϕ; we keep the diffusivity $D = \frac{\gamma\Lambda}{\xi^2}$ constant. The stability of the antibubble system (in the absence of gravity) depends on the parameters D and ξ. We have found that large values of D, along with low values of ξ, help to make the antibubble stable; $D = 0.004$ works well for our present study. Investigations

TABLE I. Parameters $R_0, R_1, h_0, \xi, \sigma, \nu, D, Ch, Sc$ for our CHNS DNS runs R1-R35. Initially, R_0 and R_1 are, respectively, the outer and inner radii of the antibubble; $h_0 \equiv (R_0 - R_1)$; σ is the surface tension; ν is the kinematic viscosity. In all the runs, the Atwood number times the acceleration due to gravity $Ag = 0.99$; the number of collocation points is N^2; the diffusivity is D; the Cahn number $Ch = \xi/L$, ξ being the interface width. The typical values of R_0/h_0 used in experiments are about 38 [22]. For all our 2D runs, the friction coefficient $\alpha = 0.001$.

	N	R_0/ξ	R_1/ξ	R_0/h_0	h_0/ξ	D	Ch	$Bo(\times 10^{-3})$	ν	Sc
R1-R20	1024 (2D)	76.6	69.7	7	6.96	0.004	0.0028	36–0.45	0.007	1.75
R21-R35	1024 (2D)	76.6	69.7	7	6.96	0.004	0.0028	12–0.45	0.001	0.25
R36-50	1024 (2D)	76.6	69.7	8	6.96	0.004	0.0028	12–0.45	0.001	1.75
R51-65	1024 (2D)	76.6	69.7	9	6.96	0.004	0.0028	12–0.45	0.001	1.75
R66-86	1024 (2D)	76.6	69.7	11	6.96	0.004	0.0028	0.01	0.007	1.75–241.7

of the thermodynamic stability of the antibubblebubbles can be found in [41–44]. However, detailed investigations with varying D lie outside the scope of the current work. As we have shown in our Supplemental Material ([45], Figs. S5 and S6), the antibubble is stable for times that are at least as long as our simulation times. At very long times, the antibubble breaks and retracts to a circular disk-like shape. We study the retraction dynamics of an antibubble by varying the Atwood number A and the Bond number $Bo = Ag\rho h_0^2/\sigma$. The Bond number is a convenient dimensionless ratio of body forces (gravity), on the antibubble, and the surface or interfacial tension σ. We express times in multiples of $\tau_g \equiv \sqrt{R_0/Ag} \simeq 1.16$, given the parameters we use. In the simulations reported in this paper, the interface width ξ is the same for all the 2D runs. Simulations with varying ξ lie outside of the scope of the present paper. Note that, due to gravity, the inertial term becomes very important and the observables reported in our study are mostly dominated by the inertial terms instead of the interfacial diffusion terms. Thus we expect the trend of the observables to converge with varying ξ.

We solve the CHNS Eqs. (1) and (2) by using the pseudospectral method with periodic boundary conditions; because of the cubic nonlinearity in the chemical potential μ, we use $N/2$ dealiasing [46]. We use the exponential Adams-Bashforth method ETD2 [47] for time marching. For our 2D DNSs, we use computers with Graphics Processing Units (e.g., the NVIDIA K80), which we program in CUDA [48]. We use conventional CPU-based computers for our 3D DNSs. We have N collocation points in each direction and our domain length is $L = 2\pi$. Our efficient code allows us to explore the CHNS parameter space and carry out very long simulations that are essential for our studies.

For the VF method we note the following points. It is a sharp-interface method, so it has $Ch = 0$. The surface tension force for VF is $\mathbf{F}_\sigma \equiv \sigma\kappa\delta_s\mathbf{n}$, where κ is the curvature, δ_s is the Dirac delta function on the interface, and $\mathbf{n}$ is the normal to the interface. We use Basilisk [49,50], an open-source solver for carrying out both 2D and 3D axisymmetric VF DNSs. Basilisk, which employs the Bell-Collela-Glaz advection scheme [51] and the implicit viscosity solver [49,50], is parallelized over conventional CPUs [49,50]. The VF solver does not invoke the Boussinesq approximation and it can handle large density and viscosity contrasts. The breakup of an interface is sensitive to the resolution in the VF, so we use an initial configuration in which the antibubble is already punctured at the bottom and we then investigate its spatiotemporal evolution. This initial condition is similar to that used in experiments and in Ref. [23]. We use the following boundary conditions in our VF simulations: (a) In our 2D DNSs we employ periodic boundary conditions in all directions; (b) in the 3D axisymmetric case we use an axisymmetric boundary condition on the $z = 0$ axis and the no-slip condition $\boldsymbol{u} = 0$ at other boundaries.

We list the parameters for some of our representative DNS runs in Tables I, II, and Table III in the Supplementary Material [45]. We also give tables with the details of all our DNSs in the Supplemental Material (in particular, see Table I, Table II, and Table IV in the Supplemental Material [45]). As we show below, by utilizing both the CHNS framework and the VF method, we can capture accurately the rupture and retraction dynamics of an antibubble in an elegant and numerically efficient way.

III. RESULTS

We now present the results of our DNSs in the following subsections: in subsection III A we illustrate the spatiotemporal evolution of 2D antibubbles and, in subsection III B, we give the temporal evolution of Fourier spectra of ϕ and the velocity and vorticity fields that are associated with these antibubbles. In subsection III C we explore the dependence on σ of the velocity of the retracting rim of a ruptured 2D antibubble and, in subsection III D, we examine the signatures of this rupture in the time dependence of the energy. Furthermore, we elucidate the dependence of the antibubble-rupture time on the size of the antibubble and the surface tension (subsection III E 1) and on the kinematic viscosity (subsection III E 2). We then present illustrative results on the spatiotemporal evolution of 3D antibubbles in subsection III F

A. Spatiotemporal evolution: 2D

In Fig. 1 we display, via pseudocolor plots of ϕ and ω, the spatiotemporal evolution of a 2D antibubble rising under gravity in our CHNS DNS; blue and red indicate heavy and light fluids, respectively. We show pseudocolor images for only two representative cases, one each from the CHNS and the VF simulations. All other cases (Tables I and II) show similar spatiotemporal evolution of an antibubble, with the only difference being the time of antibubble rupture and the velocity of the antibubble rim. Figure 1(a) shows the pseudocolor plot of ϕ for the antibubble at a time $\simeq 0$. Initially, the antibubble rises because of gravity, breaks [Fig. 1(b)], then displays arms that retract and forms a disk-shaped droplet, which rises under

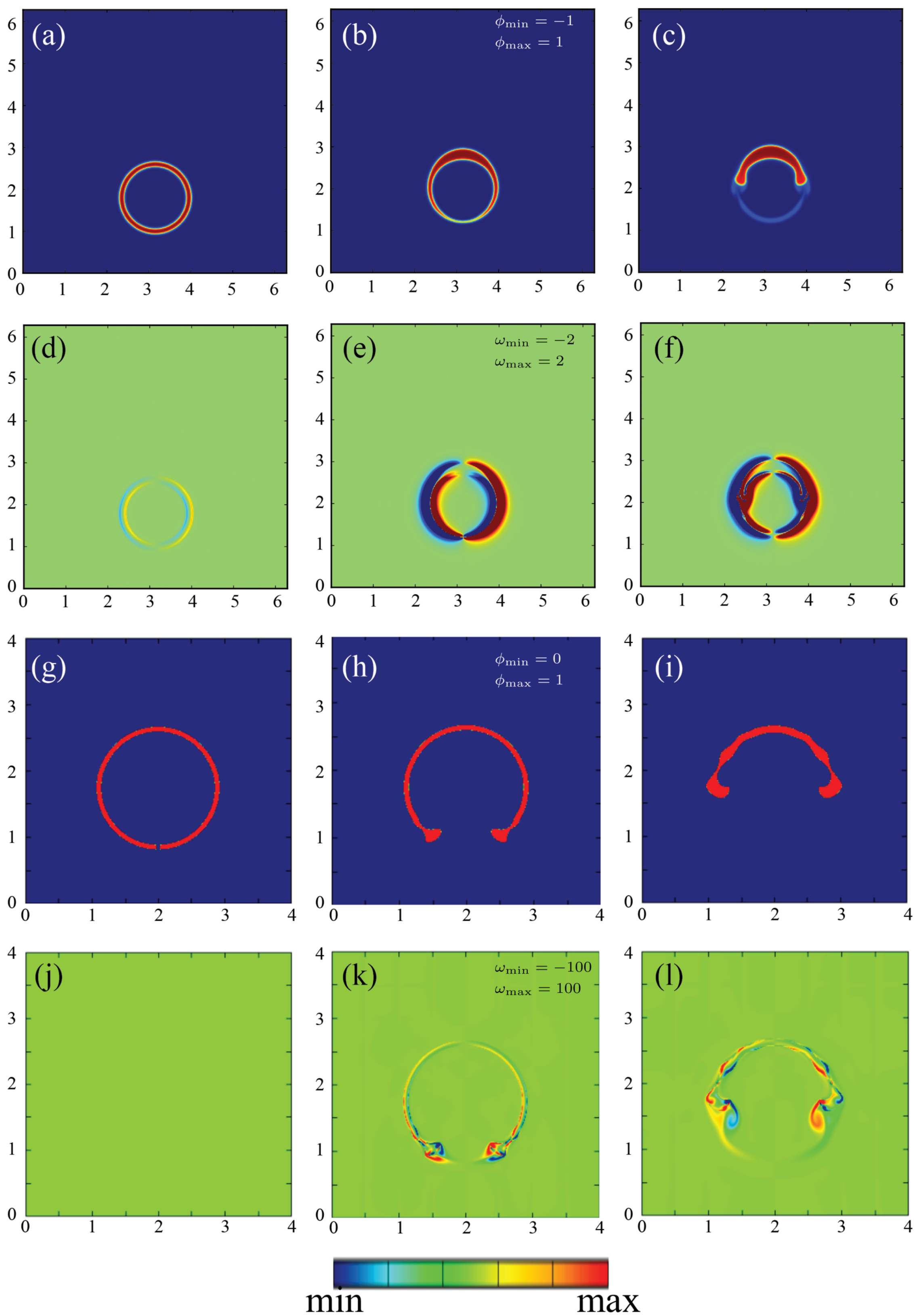

FIG. 1. Pseudocolor plots of the CHNS ϕ field with antibubble radius $R_0/h_0 = 7$ at time (a) $t = 0.0$, (b) $t = 1.74\tau_g$, and (c) $t = 2.01\tau_g$ for $\nu = 0.007$ and $\sigma = 1.66$; pseudocolor plots of the corresponding ω field (d)–(f). These plots show that, initially, the antibubble rises under gravity, breaks, (a),(d), then it retracts (b),(e), becomes a circular droplet, and rises again (e),(f). Pseudocolor plots of the volume fraction for the 2D VF run PR5 (see Table III in the Supplemental Material [45]) at time (g) $t = 0$, (h) $t = 0.1\tau_g$, and (i) $t = 0.3\tau_g$; (j), (k), and (l) pseudocolor plots of the vorticity for the 2D VF PR5 run at the same times as in (g), (h), and (i), respectively; in these 2D VF runs, $\sigma = 1.68$; these plots show that the antibubble retracts and forms a rim. Time is measured in units of τ_g.

TABLE II. Parameters $R_0, R_1, h_0, \xi, \sigma, \nu, D, Ch, Sc$ for our CHNS DNS runs Q1–Q7. Initially, R_0 and R_1 are, respectively, the outer and inner radii of the antibubble; $h_0 \equiv (R_0 - R_1)$; σ is the surface tension; ν is the kinematic viscosity. In all the runs, the Atwood number times the acceleration due to gravity $Ag = 0.5$, the number of collocation points for Q1–Q6 is $N^3 = 256^3$ and for Q7 is $N^3 = 512^3$: the diffusivity is D; the Cahn number $Ch = \xi/L$, with ξ being the interface width. The typical values of R_0/h_0 used in experiments are about 38 [22].

	N	R_0/ξ	R_1/ξ	R_0/h_0	h_0/ξ	D	Ch	$Bo(\times 10^{-3})$	ν	Sc
Q1	256 (3D)	24.0	12.0	1.2	12.0	0.006	0.013	1.3	0.0016	0.27
Q2	256 (3D)	24.0	12.0	1.2	12.0	0.006	0.013	0.63	0.0016	0.27
Q3	256 (3D)	24.0	12.0	1.2	12.0	0.006	0.013	0.4	0.0016	0.27
Q4	256 (3D)	24.0	12.0	1.2	12.0	0.006	0.013	0.3	0.0016	0.27
Q5	256 (3D)	24.0	12.0	1.2	12.0	0.006	0.013	0.25	0.0016	0.27
Q6	256 (3D)	24.0	12.0	1.2	12.0	0.006	0.013	0.21	0.0016	0.27
Q7	512 (3D)	14	10.5	4.0	3.5	0.006	0.011	2.7	0.0016	0.27

gravity [Fig. 1(c)], because the antibubble-shell (red) fluid is lighter than the background (blue) fluid. Figures 1(d)–1(f) show pseudocolor plots of the vorticity field at the same times as their ϕ counterparts in Figs. 1(a)–1(c). The spatiotemporal evolution of such a 2D antibubble is shown in videos S7 and S8 in the Supplemental Material [45]. Note that, just after forming the disk-type shape, the antibubble goes down in a direction opposite to that dictated by gravity [Fig. 1(e)], because the surface tension is high; so, during the retraction of the arms, when interfacial energy is released, the retracting droplet can be pushed in this opposite direction. Eventually this backward thrust is damped by viscosity and, finally, the (light) droplet rises under gravity. We begin with $\omega = 0$, everywhere. We see that, because of the $\nabla \times \phi \nabla \mu$ term on the right-hand side (RHS) of Eq. (3), a vorticity field is generated at the outer and inner surfaces of the antibubble, i.e., wherever ϕ changes in space. The vortical regions that are generated initially have a size that is comparable to the interface width. These vortices then grow with time, until they are damped by viscosity. Similarly, the gravity term is also significant wherever ϕ changes sign. The competition between the viscous, surface-tension, and gravity terms in the CHNS equations determines the breakup time of an antibubble, as we show below.

In Figs. 1(g)–1(l) we use pseudocolor plots to illustrate antibubble retraction in our VF DNS in 2D (run PR1 in Table IV in the Supplemental Material [45]). Both our CHNS and VF DNSs show that, as it ruptures, an antibubble forms a rim, which then retracts.

In our VF study the antibubble is punctured early in the DNS [Fig. 1(g)]; this is in contrast to the breakup by gravity-induced drainage in our CHNS DNS, which occurs in Fig. 1(b) at $\simeq 1.74\tau_g$. Thus we cannot compare the breakup times between VF and CHNS DNSs directly. We can, however, compare either the retraction velocity of the antibubble rim or the time that the rim takes to move a given distance in both CHNS and VF DNSs, which have the same surface tension (as in Fig. 1). In our CHNS DNS, the time difference between Fig. 1(c) and the antibubble-rupture time [Fig. 1(b)] is $\simeq 0.27\tau_g$; in our VF DNS, the time difference between Fig. 1(i) and the antibubble-puncture time [Fig. 1(g)] is $\simeq 0.3\tau_g$. Thus the time that the rim takes to move a given distance is approximately equal in the CHNS and VF DNS results, which we show in Fig. 1; in both these DNSs, the surface tensions are the same.

B. Fourier spectra

Fourier-space spectra give us a complementary view of the spatiotemporal evolution of the rupture of an antibubble [cf. the physical-space pseudocolor plots in Figs. 1(a)–1(l)]. In Fig. 2 we show, for our 2D CHNS DNSs, log-log (base 10) plots of the spectra for the field ϕ, the energy spectrum $E(k,t)$, and the enstrophy spectrum $\Omega(k,t)$, at different times during this evolution. These spectra are defined as follows:

$$S(k,t) \equiv \sum_{k-\frac{1}{2}\leqslant k'\leqslant k+\frac{1}{2}} \langle \hat{\phi}(\boldsymbol{k}',t)\hat{\phi}(-\boldsymbol{k}',t)\rangle,$$
$$E(k,t) \equiv \frac{1}{2}\sum_{k-\frac{1}{2}\leqslant k'\leqslant k+\frac{1}{2}} \langle \hat{\boldsymbol{u}}(\boldsymbol{k}',t)\hat{\boldsymbol{u}}(-\boldsymbol{k}',t)\rangle,$$
$$\Omega(k,t) \equiv \frac{1}{2}\sum_{k-\frac{1}{2}\leqslant k'\leqslant k+\frac{1}{2}} \langle \hat{\omega}(\boldsymbol{k}',t)\hat{\omega}(-\boldsymbol{k}',t)\rangle. \qquad (6)$$

Here, the circumflex denotes a spatial Fourier transform and k and k' are, respectively, the magnitudes of the wave vectors $\boldsymbol{k}$ and $\boldsymbol{k}'$. At early times [Figs. 2(a), 2(d) and 2(g)], these spectra, especially $S(k,t)$, show oscillations with small and large periods, which are, respectively, related inversely to the outer radius of the antibubble and the thickness of its shell. In particular, the oscillations at large k have a period of $\Delta k \simeq \frac{2\pi}{h}$, where $h = R_0 - R_1$ is the thickness of the antibubble at $t = 0$. As the antibubble ruptures [Figs. 2(b), 2(e) and 2(h)], it loses its circular shape and, in turn, the spectra lose their oscillations. Finally, the antibubble is replaced by a single droplet [Fig. 1(c)] of the light fluid, which rises under gravity; at this stage, these spectra, especially $S(k,t)$, show oscillations with a small period, which is related inversely to the radius of this rising droplet. These Fourier-space spectra show that the breakup of an antibubble leads to turbulence, insofar as $E(k,t)$, $S(k,t)$, and $\Omega(k,t)$ extend significantly over several orders of magnitude of k. The Taylor-microscale Reynolds number Re_λ is 0.54, 128.5, and 163.4 in Figs. 2(a)–2(c), respectively; here, $\mathrm{Re}_\lambda = u_{rms}\lambda/\nu$, where the root-mean-square velocity $u_{rms}(t) = 2\sum_k E(k,t)$ and the Taylor microscale $\lambda \equiv [\sum k^2 E(k,t)/\sum E(k,t)]^{-1/2}$.

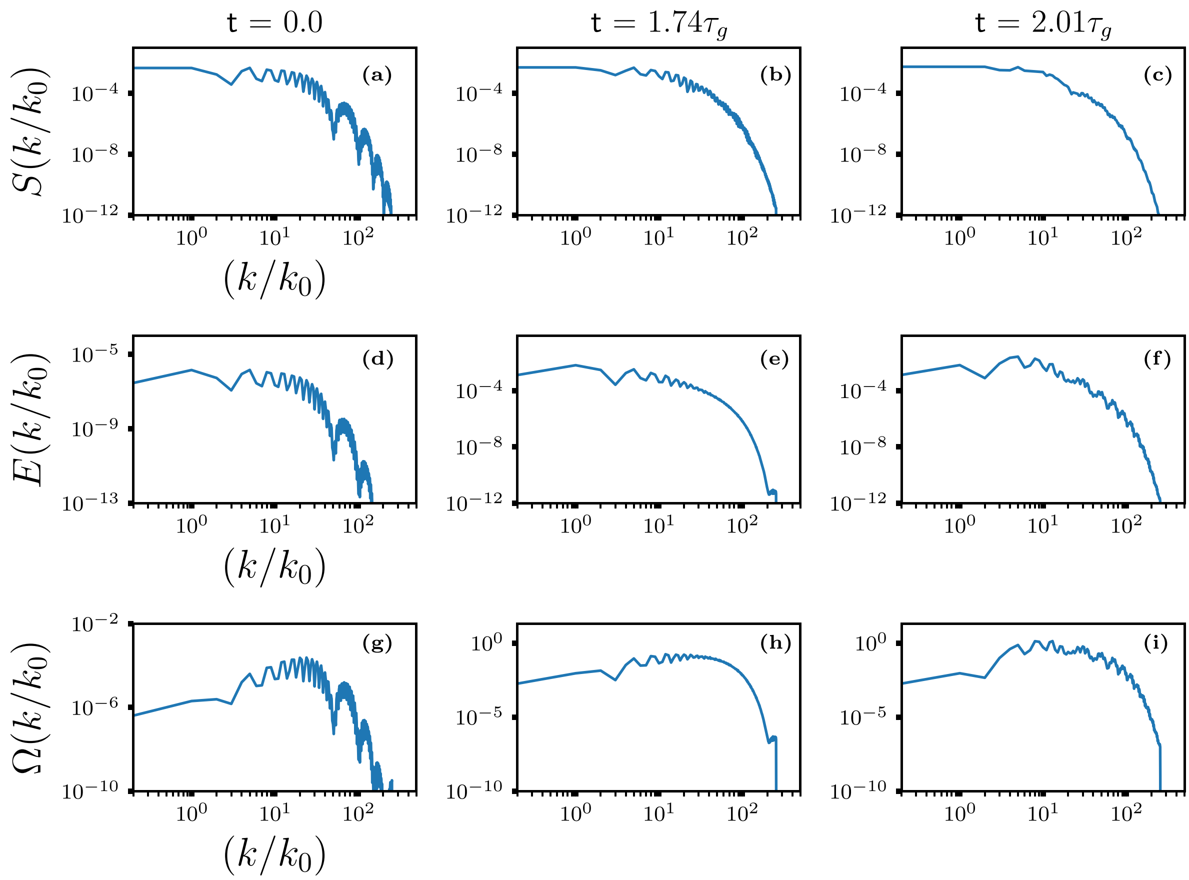

FIG. 2. Log-log (base 10) plots of the spectra [Eq. (6)] (a)–(c) $S(k,t)$, (d)–(f) $E(k,t)$, and (g)–(i) $\Omega(k,t)$ versus k, with $k_0 = 1$ and time in units of τ_g.

C. Rim-retraction velocity

When an antibubble ruptures, the surface-tension energy (the interfacial free energy in the CHNS description) is converted to the kinetic energy of the antibubble. The rate of change of the former is $\sigma\, d\mathcal{S}(t)/dt$, where $\mathcal{S}(t)$ is the outer perimeter of the antibubble in our 2D DNSs, and the kinetic energy that is released is $E_M = \int_{S_f}[\rho v^2(\boldsymbol{x},t)]d\boldsymbol{x}$, where S_f is the area of the majority phase surrounding the minority phase; this causes the film to retract. Figures 1(a)–1(l) show that, in both of our CHNS and VF DNSs, as it ruptures, an antibubble forms a rim, which then retracts. When this rim retracts, the outer perimeter of the antibubble reduces by a length R_f on one side after the rupture and, if a is the thickness of the vanished film, then $E_M = \rho v_{\rm rim}^2 a R_f$, where $v_{\rm rim}$ is the rim-retraction velocity. If we assume, furthermore, that the rim retracts with a constant velocity, then $dv_{\rm rim}/dt = 0$, so $dR_f/dt = v_{\rm rim}$. Finally, we find

$$\sigma d\mathcal{S}(t)/dt \propto dE_M/dt, \Rightarrow v_{\rm rim} = (\sigma/\rho)^{1/2}. \quad (7)$$

This dependence of $v_{\rm rim}$ on σ matches the experimental observations in Ref. [21]. Moreover, this dependence is the same in both our CHNS and VF DNSs, even though, in the former, antibubble breakup occurs because of gravity-induced thinning, whereas, in the latter, this breakup is induced by puncturing the antibubble at its bottom boundary. The puncturing initial condition has also been used in the experiments and a theory of antibubble collapse [22,23].

The plot in Fig. 3 shows that rim velocities, which we obtain from 2D CHNS and VF DNSs and our 3D axisymmetric

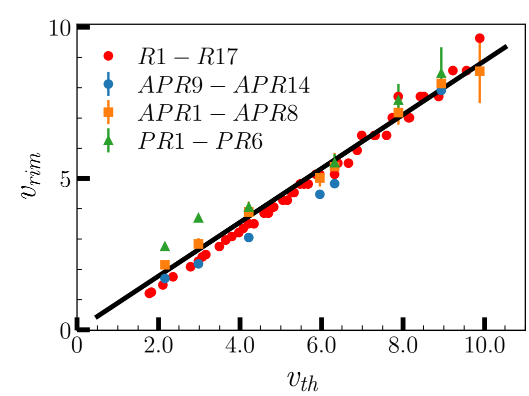

FIG. 3. Plot of the retraction velocity $v_{\rm rim}$ versus the theoretical estimate $v_{th} = \sqrt{\sigma/\rho_2 a}$ for our 2D CHNS runs R1-R17 (Table I), 2D VF runs PR1-PR6, and 3D axisymmetric VF runs APR1-APR14 (Table III in the Supplemental Material [45]); red circles show data from our CHNS runs; green, yellow, and blue markers indicate data from our VF runs. The black line represents the theoretical line. Here the surface tension $\sigma = \frac{Ag\rho h_0^2}{Bo}$, where Bo is the Bond number.

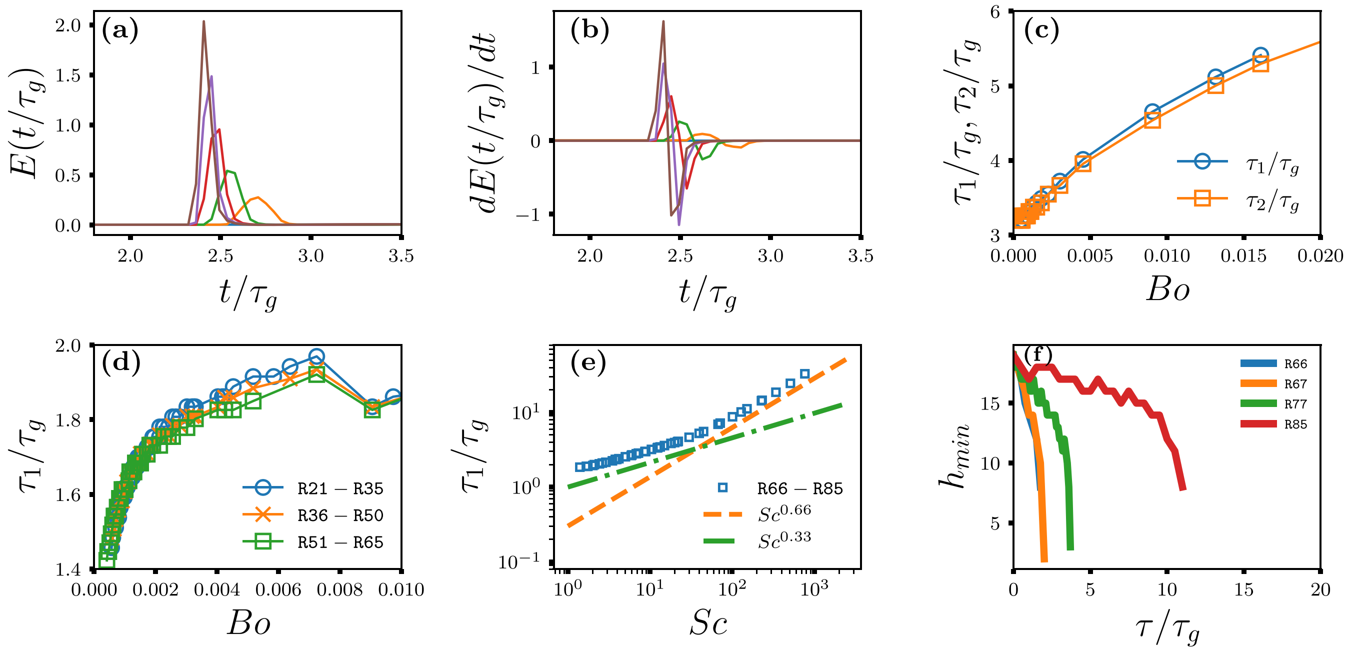

FIG. 4. Plots of (a) the total kinetic energy $E(t)$ and (b) the time derivative $dE(t)/dt$ versus t/τ_g for the 2D CHNS runs R16-R20; (c) plots versus Bo of the antibubble lifetimes τ_1 and τ_2 calculated, respectively, from the energy time series (blue line with circles) and the minimum antibubble thickness (orange line with squares), for the 2D CHNS runs R1-R16. (d) Plots versus Bo (for $Sc = 1.75$), of τ_1/τ_g for $R_0/h_0 = 7$ (DNS runs R21-R35, blue line with circles), $R_0/h_0 = 8$ (DNS runs R36-R50, orange line with crosses), $R_0/h_0 = 9$ (DNS runs R51-R65, green line with squares); (e) log-log plot of τ_1/τ_g versus Sc, over three orders of magnitude and at a fixed value of Bo (runs R66-R85); (f) plots of $h_{\min}$ versus t/τ_g, at $Bo = 0.01$ and $A = 0.01$ and $g = 99$, for $Sc = 1.75$ (R66, blue line), $Sc = 2.6$ (R67, orange line), $Sc = 20$ (R77, green line), and $Sc = 151.5$ (R84, red line). Details can be found in Tables I and II in the Supplemental Material [45].

VF runs, for both high and low A, are in excellent agreement with the theoretical prediction $v_{th} \sim \sqrt{\sigma/\rho_2 a}$ [23], where a is the radius of the rim ($a = \sqrt{h_0 R_0/\pi}$).

D. Energy time series

When an antibubble bursts, the surface tension energy is converted into the kinetic energy of the fluid; this yields a spike in the fluid-energy time series [see Fig. 4(a)]. Therefore, we identify the breakup time τ_1 as the instant at which $dE(t)/dt$ displays a maximum [see Fig. 4(b)]. We also define the breakup time τ_2 at which the antibubble-shell thickness $h_{\min}$, at the lower end of the antibubble, vanishes. In Fig. 4(c) we show plots of both τ_1 and τ_2 versus Bo for an antibubble with $R_0/h_0 = 11$ and $\nu = 0.967$. This plot shows that both our estimates of the collapse times, τ_1 and τ_2, agree with each other. (For details, see Sec. I in the Supplemental Material [45].)

E. Antibubble-breakup times

The antibubble-breakup times, which we have defined above, depend on the initial size of the antibubble, the surface tension, and the kinematic viscosity. We explore these dependences below via our 2D CHNS DNSs.

1. Dependences on size and surface tension

The size- and surface-tension dependences of the antibubble-breakup time follow from the plots of τ_1/τ_g versus Bo, which we give in Fig. 4(d), for (i) $R_0/h_0 = 7$ (DNS runs R21-R35, blue line with circles), (ii) $R_0/h_0 = 8$ (DNS runs R36-R50, orange line with crosses), and (iii) $R_0/h_0 = 9$ (DNS runs R51-R65, green line with squares). In all these plots, the viscosity is fixed and the Schmidt number $Sc = 1.75$. Although the scaling of τ_1 by $\tau_g = \sqrt{R/Ag}$ makes all the curves collapse on top of each, to a large degree, there is a small, but noticeable, difference between these curves.

2. Dependence on the kinematic viscosity

In Fig. 4(e), we present a log-log plot of τ_1/τ_g versus Sc, over three orders of magnitude and at a fixed value of Bo; clearly, τ_1/τ_g increases with Sc, with low-Sc and high-Sc asymptotes, which are consistent with $Sc^{\frac{1}{3}}$ and $Sc^{\frac{2}{3}}$.

In Fig. 4(f), we plot $h_{\min}$ versus t/τ_g, at $Bo = 0.01$, $A = 0.01$, and $g = 99$, for $Sc = 1.75$ (blue line), $Sc = 2.6$ (orange line), $Sc = 20$ (green line), and $Sc = 151.5$ (red line). We note that $h_{\min}$ falls rapidly, for $Sc = 1.75$, but falls slowly, when $Sc = 151.5$. This observation agrees with experiments [21].

F. Three-dimensional antibubbles

We now present illustrative results for 3D antibubbles evolving under gravity from our CHNS and VF runs Q1-Q7, in Table II, and APR1-APR14 in Table III in the Supplemental Material [45]), respectively. In Fig. 5(a) we give, for comparison, an image of an antibubble from an experiment (courtesy of Kalelkar from Ref. [12]). In Figs. 5(b) and 5(c) we show psuedocolor plots of two-dimensional sections of ϕ

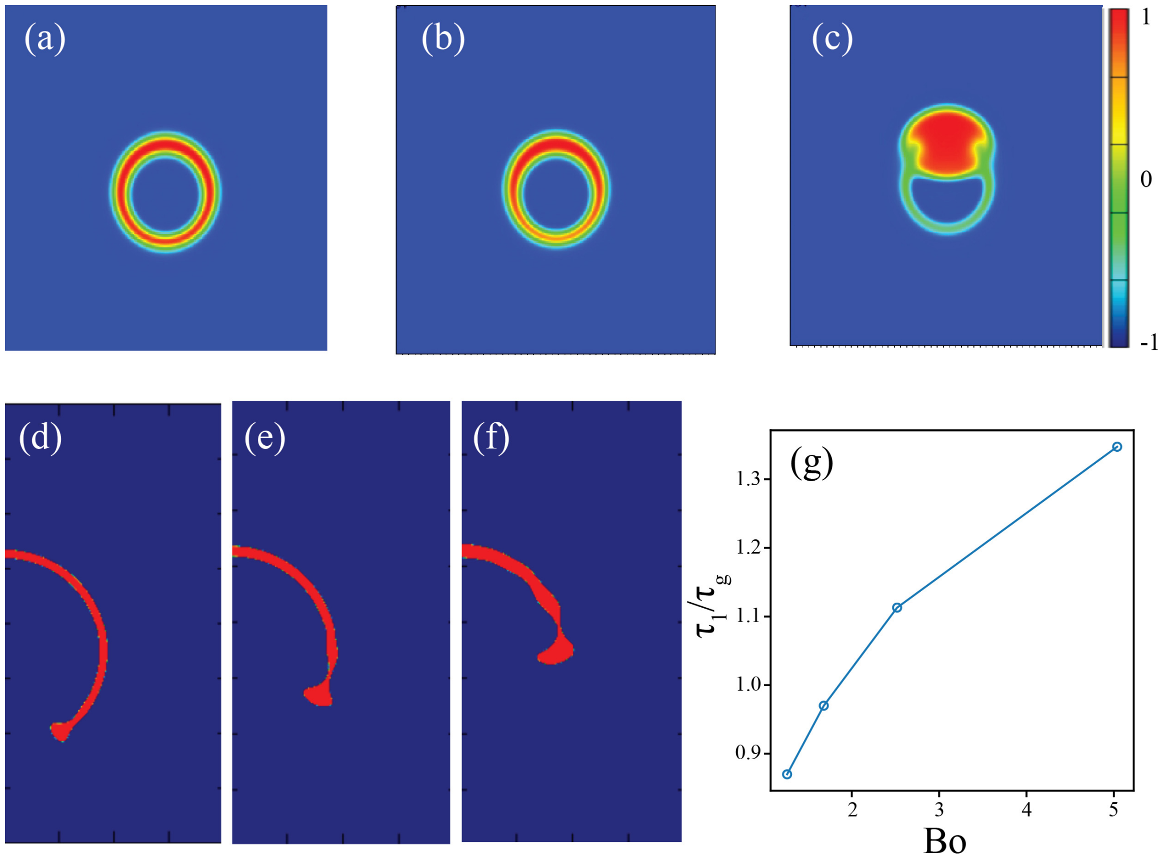

FIG. 5. Pseudocolor plot of order parameter showing a section at $y = \pi$ from 3D simulations of antibubbles from run R2 at (a) $t = 0.1\tau_g$; (b) $t = 0.2\tau_g$ and (c) $t = 0.3\tau_g$; pseudocolor plots of ϕ from our 3D axisymmetric VF run APR7 at (d) $t = 0$, (e) $t = 0.1\tau_g$, and (f) $t = 0.3\tau_g$ showing majority (blue) and minority (red) phases; (g) plot of τ_1/τ_g versus Bo from our 3D CHNS runs Q1–Q6.

(with $y = \pi$ in our 3D CHNS run R2) at (b) $t = 0.1\tau_g$ and (c) $t = 0.3\tau_g$. We see that the South pole of the antibubble becomes thinner, with the passage of time, while a dome develops at its North pole. We also find that, at least for the parameters we use, the initially spherical antibubble remains axisymmetric. Therefore, we design our 3D VF simulations to be axisymmetric. In Figs. 5(d) and 5(e) we show the rupture of an antibubble in our 3D axisymmetric APR7 VF run at (d) $t = 0$, (e) $t = 0.1\tau_g$, and (f) $t = 0.3\tau_g$.

As we did in our 2D CHNS studies, we identify the antibubble-breakup time τ_1 as the time when dE/dt reaches its maximum value. In Fig. 5(g) we plot τ_1/τ_g versus Bo for our 3D CHNS runs Q1–Q6; we find that this plot is qualitatively similar to its 2D CHNS counterpart in Fig. 4(b). We recall that the plot in Fig. 3(b) also shows that rim velocities, which we obtain from 3D axisymmetric VF runs, are in excellent agreement with the theoretical prediction [23].

IV. CONCLUSIONS

An experimental study [7] has the title *Vita brevis* (Latin for *short life*) of antibubbles. We have shown how to use the CHNS system for studying the spatiotemporal evolution of this *short life* of antibubbles, in both 2D and 3D. Our DNSs of the CHNS system allow us to study, numerically and theoretically, the collapse or breakup of an antibubble because of the gravity-induced thinning at its South pole. This occurs in experiments via the drainage of air from the lower end of the antibubble. In some experiments, where antibubbles are stabilized, say by the addition of surfactants, antibubble rupture is precipitated by piercing its shell; we have studied such rupture via the VF method. By considering Fourier-space spectra, we have shown that the breakup of an antibubble leads to turbulence, insofar as these spectra have significant weight over several orders of magnitude of wave numbers. Our DNSs have allowed us to study the dependence of the antibubble lifetime on the surface tension, which is related inversely to the Bond number Bo, the kinematic viscosity, which is related directly to the Schmidt number Sc, and the ratio R_0/h_0 of the initial antibubble radius R_0 and its thickness h_0. We have also shown how the antibubble-rim-retraction velocity depends on the surface tension, in both CHNS and VF DNSs.

The dependence of the antibubble lifetime on the surface tension has been studied earlier [21], through experiments and numerical simulation of the balance equations obtained from lubrication theory. A recent study [24] uses the Allen-Cahn-Navier-Stokes equations, with order-parameter conservation enforced numerically via a Lagrange multiplier. Our work extends significantly theoretical and DNS studies of antibubbles, by using the CHNS system, in which order-parameter conservation is built in manifestly, and the VF method that can be used fruitfully if interfaces are very thin and non-

Boussinesq effects are present. Our results agree with earlier results, where they exist. The number of studies on antibubbles is limited partly because great care has to be exercised to stabilize antibubbles in terrestrial (as opposed to zero-gravity) experiments. Often a surfactant has to be introduced into the high-density liquid phase for such stabilization. We hope our detailed study of the spatiotemporal evolution of antibubbles, from their initiation to their rupture, and of their effect on the background fluid, will lead to more experimental studies of the properties of these ephemeral, but beautiful, inverted bubbles.

ACKNOWLEDGMENTS

We thank C. Kalelkar for introducing us to experimental studies of antibubbles [12]. We thank N. B. Padhan and S. Sarkar for discussions. P.P. and R.R. acknowledge support from intramural funds at TIFR Hyderabad from the Department of Atomic Energy (DAE), India and DST (India) Project No. ECR/2018/001135; N.P., R.P. thanks CSIRi, SERB, and the National Supercomputing Mission (India) for support and SERC (IISc) for computational resources.

[1] W. Hughes and A. R. Hughes, Liquid drops on the same liquid surface, Nature (London) **129**, 59 (1932).

[2] S. Kotopoulis, A. Delalande, M. Popa, V. Mamaeva, G. Dimcevski, O. H. Gilja, M. Postema, B. T. Gjertsen, and E. McCormack, Sonoporation-enhanced chemotherapy significantly reduces primary tumour burden in an orthotopic pancreatic cancer xenograft, Mol. Imaging Biol. **16**, 53 (2014).

[3] K. Johansen, S. Kotopoulis, A. T. Poortinga, and M. Postema, Nonlinear echoes from encapsulated antibubbles, Phys. Procedia **70**, 1079 (2015).

[4] S. Kotopoulisa, K. Johansenb, O. H. Giljaa, A. T. Poortingad, and M. Postemab, Acoustically active antibubbles, Acta Physica Polonica A **127**(1), 99 (2015).

[5] M. Postema and O. H. Gilja, Ultrasound-directed drug delivery, Curr. Pharm. Biotechnol. **8**, 355 (2007).

[6] K. Johansen, S. Kotopoulis, and M. Postema, Ultrasonically driven antibubbles encapsulated by Newtonian fluids for active leakage detection, in *Proceedings of the International Multi-Conference of Engineers and Computer Scientists, Hong Kong*, Vol II, Lecture Notes in Engineering and Computer Science (IMECS, 2015), pp. 750–754.

[7] S. Dorbolo, N. Vandewalle, E. Reyssat, and D. Quéré, Vita brevis of antibubbles, Europhys. News **37**, 24 (2006).

[8] P. G. Kim and J. Vogel, Antibubbles: factors that affect their stability, Colloids Surf., A **289**, 237 (2006).

[9] S. Dorbolo, D. Terwagne, R. Delhalle, J. Dujardin, N. Huet, N. Vandewalle, and N. Denkov, Antibubble lifetime: Influence of the bulk viscosity and of the surface modulus of the mixture, Colloids Surf., A **365**, 43 (2010).

[10] S. Dorbolo, H. Caps, and N. Vandewalle, Fluid instabilities in the birth and death of antibubbles, New J. Phys. **5**, 161 (2003).

[11] L. Bai, W. Xu, P. Wu, W. Lin, C. Li, and D. Xu, Formation of antibubbles and multilayer antibubbles, Colloids Surf., A **509**, 334 (2016).

[12] C. Kalelkar, The inveterate tinkerer, Resonance **22**, 955 (2017).

[13] E. Chatzigiannakis, N. Jaensson, and J. Vermant, Thin liquid films: where hydrodynamics, capillarity, surface stresses, and intermolecular forces meet, Curr. Opin. Colloid Interface Sci. **53**, 101441 (2021).

[14] E. Chatzigiannakis and J. Vermant, Breakup of Thin Liquid Films: From Stochastic to Deterministic, Phys. Rev. Lett. **125**, 158001 (2020).

[15] Y. Song, L. Zhang, and E. N. Wang, Criteria for antibubble formation from drop pairs impinging on a free surface, Phys. Rev. Fluids **5**, 123601 (2020).

[16] J. B. Will, V. Mathai, S. G. Huisman, D. Lohse, C. Sun, and D. Krug, Kinematics and dynamics of freely rising spheroids at high reynolds numbers, J. Fluid Mech. **912**, A16 (2021).

[17] Y. Li, C. Diddens, A. Prosperetti, and D. Lohse, Marangoni Instability of a Drop in a Stably Stratified Liquid, Phys. Rev. Lett. **126**, 124502 (2021).

[18] Á. MorenoSoto, P. Peñas, G. Lajoinie, D. Lohse, and D. van der Meer, Ultrasound-enhanced mass transfer during single-bubble diffusive growth, Phys. Rev. Fluids **5**, 063605 (2020).

[19] Á. M. Soto, D. Lohse, and D. van der Meer, Diffusive growth of successive bubbles in confinement, J. Fluid Mech. **882**, A6 (2020).

[20] V. N. Prakash, J. M. Mercado, L. van Wijngaarden, E. Mancilla, Y. Tagawa, D. Lohse, and C. Sun, Energy spectra in turbulent bubbly flows, J. Fluid Mech. **791**, 174 (2016).

[21] B. Scheid, S. Dorbolo, L. R. Arriaga, and E. Rio, Antibubble Dynamics: The Drainage of an Air Film with Viscous Interfaces, Phys. Rev. Lett. **109**, 264502 (2012).

[22] J. Zou, C. Ji, B. G. Yuan, X. D. Ruan, and X. Fu, Collapse of an antibubble, Phys. Rev. E **87**, 061002(R) (2013).

[23] D. N. Sob'yanin, Theory of the Antibubble Collapse, Phys. Rev. Lett. **114**, 104501 (2015).

[24] J. Yang, Y. Li, D. Jeong, and J. Kim, Mathematical modeling and simulation of antibubble dynamics, NMTMA **13**, 81 (2019).

[25] Y. Vitry, S. Dorbolo, J. Vermant, and B. Scheid, Controlling the lifetime of antibubbles, Adv. Colloid Interface Sci. **270**, 73 (2019).

[26] G. Boffetta and R. E. Ecke, Two-dimensional turbulence, Annu. Rev. Fluid Mech. **44**, 427 (2012).

[27] P. Perlekar, R. Benzi, H. J. H. Clercx, D. R. Nelson, and F. Toschi, Spinodal Decomposition in Homogeneous and Isotropic Turbulence, Phys. Rev. Lett. **112**, 014502 (2014).

[28] L. Scarbolo, D. Molin, P. Perlekar, M. Sbragaglia, A. Soldati, and F. Toschi, Unified framework for a side-by-side comparison of different multicomponent algorithms: Lattice boltzmann vs. phase field model, J. Comput. Phys. **234**, 263 (2013).

[29] N. Pal, P. Perlekar, A. Gupta, and R. Pandit, Binary-fluid turbulence: Signatures of multifractal droplet dynamics and dissipation reduction, Phys. Rev. E **93**, 063115 (2016).

[30] P. Perlekar, N. Pal, and R. Pandit, Two-dimensional turbulence in symmetric binary-fluid mixtures: Coarsening arrest by the inverse cascade, Sci. Rep. **7**, 44589 (2017).

[31] J. D. Gibbon, N. Pal, A. Gupta, and R. Pandit, Regularity criterion for solutions of the three-dimensional Cahn-Hilliard-

Navier-Stokes equations and associated computations, Phys. Rev. E **94**, 063103 (2016).

[32] J. D. Gibbon, A. Gupta, N. Pal, and R. Pandit, The role of bkm-type theorems in 3*d* euler, navier–stokes and cahn–hilliard–navier–stokes analysis, Physica D **376**, 60 (2018).

[33] X. Fan, P. H. Diamond, L. Chacón, and H. Li, Cascades and spectra of a turbulent spinodal decomposition in two-dimensional symmetric binary liquid mixtures, Phys. Rev. Fluids **1**, 054403 (2016).

[34] X. Fan, P. H. Diamond, and L. Chacón, Formation and evolution of target patterns in Cahn-Hilliard flows, Phys. Rev. E **96**, 041101(R) (2017).

[35] X. Fan, P. H. Diamond, and L. Chacón, Chns: A case study of turbulence in elastic media, Phys. Plasmas **25**, 055702 (2018).

[36] A. Celani, A. Mazzino, P. Muratore-Ginanneschi, and L. Vozella, Phase-field model for the rayleigh–taylor instability of immiscible fluids, J. Fluid Mech. **622**, 115 (2009).

[37] L. Scarbolo and A. Soldati, Turbulence modulation across the interface of a large deformable drop, J. Turbulence **14**, 27 (2013).

[38] P. Yue, J. J. Feng, C. Liu, and J. Shen, A diffuse-interface method for simulating two-phase flows of complex fluids, J. Fluid Mech. **515**, 293 (2004).

[39] L. Scarbolo, D. Molin, and A. Soldati, Phase field model simulation of droplet deformation and breakup in wall bounded turbulence, in *APS Division of Fluid Dynamics Meeting Abstracts* (2011).

[40] R. Pandit, P. Perlekar, and S. S. Ray, Statistical properties of turbulence: an overview, Pramana **73**, 157 (2009).

[41] D. Marti, Y. Krüger, D. Fleitmann, M. Frenz, and J. Rička, The effect of surface tension on liquid–gas equilibria in isochoric systems and its application to fluid inclusions, Fluid Phase Equilib. **314**, 13 (2012).

[42] O. Vincent and P. Marmottant, On the statics and dynamics of fully confined bubbles, J. Fluid Mech. **827**, 194 (2017).

[43] M. Gallo, F. Magaletti, and C. M. Casciola, Heterogeneous bubble nucleation dynamics, J. Fluid Mech. **906**, A20 (2021).

[44] F. Magaletti, M. Gallo, and C. M. Casciola, Water cavitation from ambient to high temperatures, Sci. Rep. **11**, 20801 (2021).

[45] See Supplemental Material at http://link.aps.org/supplemental/10.1103/PhysRevResearch.4.043128 for further details of the dynamics of the system of an antibubble rising under gravity.

[46] C. Canuto, M. Y. Hussaini, A. Quarteroni, A. Thomas, Jr. *et al.*, *Spectral Methods in Fluid Dynamics* (Springer Science & Business Media, New York, 2012).

[47] S. M. Cox and P. C. Matthews, Exponential time differencing for stiff systems, J. Comput. Phys. **176**, 430 (2002).

[48] http://www.nvidia.com/object/cuda_home_new.html.

[49] http://basilisk.fr.

[50] S. Popinet, Numerical models of surface tension, Annu. Rev. Fluid Mech. **50**, 49 (2018).

[51] J. B. Bell, P. Colella, and H. M. Glaz, A second-order projection method for the incompressible navier-stokes equations, J. Comput. Phys. **85**, 257 (1989).